Asian Journal of Pharmaceutical Sciences 16 (2021) 222–235

Available online at www.sciencedirect.com

ScienceDirect

journal homepage: www.elsevier.com/locate/AJPS

Original Research Paper

Heterobifunctional PEG-grafted black phosphorus quantum dots: "Three-in-One" nano-platforms for mitochondria-targeted photothermal cancer therapy

Junyang Qi[a], *Yue Xiong*[a], *Ke Cheng*[b], *Qi Huang*[a], *Jingxiu Cao*[a], *Fumei He*[a], *Lin Mei*[a,c,*], *Gan Liu*[a,d,*], *Wenbin Deng*[a,*]

[a] *School of Pharmaceutical Sciences (Shenzhen), Sun Yat-sen University, Shenzhen 518107, China*
[b] *Department of Chemistry, City University of Hong Kong, Hong Kong, China*
[c] *School of Material Science and Engineering and Institute for Advanced Study, Nanchang University, Nanchang 330031, China*
[d] *Department of Biochemistry and Molecular Medicine, School of Medicine, University of California at Davis, Sacramento CA 95817, USA*

ARTICLE INFO

Article history:
Received 20 March 2020
Revised 11 August 2020
Accepted 2 September 2020
Available online 18 October 2020

Keywords:
Mitochondria-target
Black phosphorus quantum dots
Photothermal therapy
Heterobifunctional PEG
Three-in-one

ABSTRACT

Black phosphorus (BP) nano-materials, especially BP quantum dots (BPQDs), performs outstanding photothermal antitumor effects, excellent biocompatibility and biodegradability. However, there are several challenges to overcome before offering real benefits, such as poor stability, poor dispersibility as well as difficulty in tailoring other functions. Here, a "three-in-one" mitochondria-targeted BP nano-platform, called as BPQD-PEG-TPP, was designed. In this nano-platform, BPQDs were covalently grafted with a heterobifunctional PEG, in which one end was an aryl diazo group capable of reacting with BPQDs to form a covalent bond and the other end was a mitochondria-targeted triphenylphosphine (TPP) group. In addition to its excellent near-infrared photothermal properties, BPQD-PEG-TPP had much enhanced stability and dispersibility under physiological conditions, efficient mitochondria targeting and promoted ROS production through a photothermal effect. Both *in vitro and in vivo* experiments demonstrated that BPQD-PEG-TPP performed much superior photothermal cytotoxicity than BPQDs and BPQD-PEG as the mitochondria targeted PTT. Thus this "three-in-one" nanoplatform fabricated through polymer grafting, with excellent stability, dispersibility and negligible side effects, might be a promising strategy for mitochondria-targeted photothermal cancer therapy.

* Corresponding authors.
E-mail addresses: meilin7@mail.sysu.edu.cn (L. Mei), liugan5@mail.sysu.edu.cn (G. Liu), dengwb5@mail.sysu.edu.cn (W. Deng).
Peer review under responsibility of Shenyang Pharmaceutical University.

https://doi.org/10.1016/j.ajps.2020.09.001

1. Introduction

In recent years photothermal therapy (PTT) has been considered as a promising alternative or supplement approach of traditional cancer treatments due to its non-invasive property and high antitumor efficacy [1–5]. Black phosphorus (BP), as a new two-dimensional material, has been an up-rising star of near infrared (NIR) photothermal agents (PTAs) in the treatment of cancer in the last years due to its excellent optical properties [6–8], good biodegradability [9] and biocompatibility [10,11]. In particular, ultrasmall BP quantum dots (BPQDs), with an approximate size of 5 nm, have many advantages, such as large extinction coefficient, high photothermal conversion efficiency [12], and efficient renal excretion [13]. With such significant advantages, however, there are two main inevitably weaknesses for BP nano-materials. The first one is that BP materials, especially BPQDs, are too fragile and easy to degrade in air-exposed water environments [14] through reacting with oxygen and water [15], which highly lowers their PTT efficacy. Another huge obstacle is the pretty bad dispersibility of BP, which makes it aggregate readily under physiological conditions. It has been recently reported that surface covalent or noncovalent functionalization with small molecule compounds and coordination with transitional metal ion can stabilize BP [16–20], but they have rarely positive effect on dispersibility. On the other hand, current conventional method to improve dispersibility of BP is to modify its surface with PEG-NH_2 by electrostatic adsorption [8]. However, BP/PEG is not dispersible enough under physiological conditions and can even disassociate easily after cell uptake. Moreover, BPQDs were also reported to be encapsulated by poly (lactic-co-glycolic acid) (PLGA) with enhanced stability and dispersibility [10], but the encapsulation efficiency is low and difficult to control. Therefore, it is of great significance to explore a novel method to enhance the stability and dispersibility of BPQDs for *in vivo* applications.

In the past decades, covalently grafting PEG on the surface of inorganic nanomaterials including nanographene and quantum dots has been investigated extensively to improve their dispersibility under physiological conditions [21–24]. On the other hand, Hersam et al. reported that the aryl diazo (AD) group can react with the P atom of the BP to form covalent bonds and significantly enhance the stability of BP [25]. Therefore, it can be speculated that AD group-terminated PEG could be grafted on the surface of BPQDs and simultaneously enhance their stability and dispersibility. Furthermore, PEG-grafting can also tailor BPQDs with additional groups for attractive functions, such as triphenyl phosphine (TPP) for mitochondria targeting. Mitochondria targeting strategy is considered as a powerful approach for enhanced PTT as mitochondria are more sensitive to heat than other parts of cells [26–29]. The grafting of PEG containing both AD and TPP groups on the surface of BPQDs is anticipated to enable efficient mitochondria targeting of BPQDs. To our knowledge, no studies have reported a simple approach that simultaneously enhances the stability, dispersibility and mitochondria targeting of BPQDs.

Herein, a heterobifunctional PEG (AD-PEG-TPP) containing both AD and TPP was designed to graft on BPQDs through a covalent bond to form the mitochondria-targeted BP nano-platform BPQD-PEG-TPP. This simple polymer-grafting strategy led to enhanced stability, dispersibility and mitochondria targeting as "three-in-one" for BPQDs under physiological conditions. *In vitro* cytotoxicity results and apoptosis mechanism demonstrated that BPQD-PEG-TPP performed much superior photothermal cytotoxicity than BPQDs and BPQD-PEG as the mitochondria targeted PTT. Furthermore, *in vivo* results confirmed it would accumulate efficiently in tumor and cause photothermal tumor ablation.

2. Material and methods

2.1. Materials

BP powder was purchased from Nanjing MKNANO Tec Co., Ltd. (Nanjing, China). AD-PEG-TPP was provided by Shanghai 9i Technology Co., Ltd. (Shanghai, China). Phosphate buffered saline (PBS), Dulbecco's modified Eagle's medium (DMEM), Fetal Bovine Serum (FBS), DiO, Lyso Tracker Green and Mito tracker Green were supplied by ThermoFisher Scientific (Australia). Hoechst 33342 was gained from Meilun Biotechnology Co., Ltd. (Dalian, China). Cell Counting Kit-8 (CCK-8) was purchased from ApexBio (Texas, USA). Dead Cell Apoptosis Kit (Annexin V-FITC), propidium iodide (PI), Calcein-AM/PI, 2′,7′-dichlorofluorescein diacetate (DCFH-DA), PI/RNase A dye working fluid were obtained from Nanjing KeyGen Biotech. Co. Ltd. (Nanjing, China). All other chemicals, unless noted, were bought from Macklin Reagents Co., Ltd. (Shanghai, China).

2.2. Preparation of BPQDs

Bulk BP powder was added into 1-methyl-2-pyrrolidone (NMP) solution in a ratio of 0.5 mg:1 ml and the mixture were sonicated in ice water for 9 h (On/Off cycle: 5 s/5 s), followed by ice-bath sonication for 10 h. The resulting dispersion was centrifuged at 14 000 rpm for 20 min and 20 000 rpm for another 20 min to precipitate the BPQDs from NMP. The concentration of P was determined by ICP-AES (7000DV, PerkinElmer). Transmission electron microscopy (TEM) and Atomic force microscopy (AFM) were used to characterize the morphology of BPQDs. TEM images was performed on a JEOL 2100 microscope operated at 120 kV. AFM was carried out on Bruker Dimension® Icon™ microscope.

2.3. Covalent grafting of BPQDs

BPQD-PEG-TPP was synthesized according to a literature reported [19,25]. AD-PEG-TPP (Shanghai 9i Technology Co., Ltd.) was added to the BPQDs solution in CH_3CN with 100 mM tetrabutylammonium hexafluorophosphate ($[Bu_4N]^+PF_6$) in a ratio of 3:1, and the mixture was shaken in the dark for 24 h. Then the mixture was centrifuged at 20 000 rpm for 20 min, and the sediment was washed with CH_3CN, ethanol,

and water. Subsequently, BPQD-PEG-TPP was resuspended in DI water or cell culture medium for further use. BPQD-PEG, NB-BPQD-PEG and NB-BPQD-PEG-TPP were also prepared in a similar manner. In addition, for *in vivo* imaging agents IR780 loading, 4.0 μg/ml of BP-PEG-TPP was mixed with IR780 (10 μg/ml) in NMP and then stirred at room temperature for 12 h. The excess unloading was washed away via rinsing with NMP, CH_3CN, ethanol and water.

Covalent grafting efficiency was defined as the weight ratio of grafted AD-PEG-TPP to BPQDs (× 100%). The concentration of unbounded AD-PEG-TPP in various AD-PEG-TPP/BPQDs feeding weight ratios (0.2, 0.5, 1.0, 2.0, 3.0, 5.0) was detected by UV–vis spectrophotometry Lambda 365 (PerkinElmer) at room temperature according to the standard curve of AD-PEG-TPP. By further conversion, the amount of AD-PEG-TPP bound with BPQDs was obtained.

2.4. Photothermal performance of BPQDs-based nano-materials

An amount of 4.0 μg/ml of each of the three BPQDs-based nano-materials (BPQDs, BPQD-PEG, BPQD-PEG-TPP) were dispersed in air-exposed water for 0, 12, 24, 48 and 72 h. The photothermal stability of these BPQDs-based nanomaterials was tested by recording the temperature change with an infrared thermal imaging camera (Ti450, Fluke, USA) under 808 nm NIR laser irradiation (BOHR-808-FCIR8, Xi'an Bohr Optoelectronics Technology Co., Ltd., China) with a power density of 1.0 W/cm^2 for 10 min at each corresponding time. Moreover, the photothermal heating effect of BPQD-PEG-TPP was determined by measuring the temperature change in DI water containing various concentrations of BPQDs (0–5.0 μg/ml) under the NIR laser irradiation with three different power density (0.5, 1.0, 1.5 W/cm^2). To further evaluate the photothermal stability of the BPQD-PEG-TPP, five temperature cycles were monitored over time, upon irradiation with an NIR laser for 10 min or under natural cooling to room temperature after the laser was turned off. The stability of the BPQDs, BPQD-PEG and BPQD-PEG-TPP in physiological medium was also established in DI water, PBS and DMEM supplemented with 10% FBS at 25 °C.

2.5. Photothermal effect tests of BPQDs-based nano-materials

The photothermal conversion efficiency (η) of BPQD, BPQD-PEG, BPQD-PEG-TPP were calculated according the following Eq. 1:

$$\eta = \frac{hS(T_{max} - T_{surr}) - Q_{dis}}{I\left(1 - 10^{-A808}\right)} \tag{1}$$

where $T_{max(BPQD)}$, $T_{max(BPQD\text{-}PEG)}$, $T_{max(BPQD\text{-}PEG\text{-}TPP)}$ were 51.9 °C, 53.3 °C, 53.6 °C, respectively. T_{surr} was the surrounding temperature of environment (26 °C). I was the laser power (I = 1.0 W/cm^2), and the A_{808} was the sample absorbance intensity at 808 nm. Q_{dis} was measured at about 808 nm was 0.54 mW.

hS was calculated according to Eq. 2:

$$\mathrm{hS} = \frac{mC}{\tau_s} \tag{2}$$

where h and S represented the heat transfer coefficient and the surface area of the container. m was the mass of the solution containing the photoactive materials and C was the heat capacity (4.2 J/g) of the DI water utilized to dissolve the materials.

τ_s was calculated according to Eq. 3:

$$\mathrm{t} = -\tau_s \ln(\theta) \tag{3}$$

where τ_s was the time constant which was calculated by the linear fitting of t versus $-ln(\theta)$.

θ was calculated according to Eq. 4:

$$\theta = \frac{T - T_{surr}}{T_{max} - T_{surr}} \tag{4}$$

where θ was the dimensionless driving force, and T was the solution temperature.

2.6. Cell culture

Human cervical cancer cell line (HeLa cells), Human Dermal Fibroblasts (HDF cells) and Human breast adenocarcinoma cells (MCF-7) were brought from ATCC, cultured in DMEM containing 10% FBS and 1% antibiotics and incubated at 37 °C in a humidified atmosphere of 5% CO_2.

2.7. In vitro co-localization of NB-BPQD-PEG-TPP into mitochondria

HeLa cells were seeded in confocal dishes (1×10^6 cells/well) and incubated overnight. Afterwards, cells were cultured with NB-BPQD-PEG-TPP (BPQD concentration of 2.0 μg/ml) and incubated for 4 h. Then, cells were washed with PBS 3 times and stained with DiO, Lyso Tracker Green, Hoechst 33342 or Mito tracker Green. After PBS washing, all samples were examined by confocal laser scanning microscope (CLSM, LSM 880 Basic Operation, Carl Zeiss). We also used MCF-7 to investigate the mitochondria co-localization in a similar protocol.

2.8. CCK-8 assay

The phototherapeutic effect of BPQD-PEG-TPP was quantified by measuring the viability of HeLa cells using CCK-8 assay. The cytotoxicity of freshly prepared BPQDs-based nanomaterials was tested in both HDF and HeLa cells. HDF cells were seeded into 96-well plates (1×10^4 cells/well) and incubated overnight. Then, HDF cells were cultured with BPQDs, BPQD-PEG and BPQD-PEG-TPP (internal BPQDs concentration of 0, 1.0, 2.0, 4.0, 10.0 μg/ml) for 24 h without irradiation before the assay. HeLa cells were also cultured with BPQDs, BPQD-PEG and BPQD-PEG-TPP (internal BPQDs concentration of 0, 0.2, 0.4, 1.0, 2.0, 4.0 μg/ml) for 24 h without irradiation. For the NIR irradiation group, HeLa cells were cultured with same concentration gradient for 4 h followed by NIR irradiation

(808 nm, 1.0 W/cm^2, 10 min), and then the cells were further incubated at 37 °C for another 24 h and cell viability was quantified using CCK-8 and reading the formazan absorbance at 450 nm by a VICTOR Nivo^{TM} Multimode Plate Reader (PerkinElmer).

2.9. Apoptosis assay

Annexin V-FITC and PI were used to detect apoptotic and necrotic cells, respectively. HeLa cells were seeded into 12-well plates (5×10^4 cells/well) and incubated overnight. Cells were treated with PBS, BPQDs, BPQD-PEG and BPQD-PEG-TPP (BPQDs concentration of 4.0 μg/ml) for 24 h followed by NIR irradiation for 4 h (808 nm, 1.0 W/cm^2, 10 min) or without irradiation. Cells were incubated for another 12 h, then washed and harvested. Apoptosis was quantified using NovoCyte 2060R (ACEA).

2.10. Calcein-AM/PI assay

Calcein-AM/PI was used to evaluate the phototherapeutic effect of BPQDs formulations. Briefly, HeLa cells were seeded into 12-well plates (1×10^5 cells/well) and incubated overnight. Subsequently, cells were cultured with BPQDs, BPQD-PEG and BPQD-PEG-TPP (internal BPQDs concentration of 4.0 μg/ml) for 24 h followed by NIR irradiation for 4 h (808 nm, 1.0 W/cm^2, 10 min) or without irradiation. After irradiation, cells were cultured at 37 °C for another 12 h, then Calcein-AM/PI was used to co-stain the cells to explore the phototherapeutic effect by a fluorescence microscope (ECLIPSE Ti2, NIKON).

2.11. ROS level measurement

DCFH-DA was used to determine the generation of intracellular ROS, which was quantified by fluorescence intensity detected by flow cytometry. HeLa cells were seeded into 12-well plates (5×10^4 cells/well) and incubated overnight. Subsequently, cells were cultured with BPQDs, BPQD-PEG and BPQD-PEG-TPP (internal BPQDs concentration of 2.0 μg/ml) and incubated for 4 h. Then, cells were washed with PBS, and cultured with H_2DCFDA (1 ml, 10 μM) for 20 min in the dark. Thereafter, cells were irradiated with NIR laser for 10 min (808 nm, 1 W/cm^2). Finally, cells were rinsed with PBS, resuspended by trypsinization, and the fluorescence intensity was immediately measured.

2.12. Cell cycle evaluation

HDF and Hela cells were seeded into 12-well plates (5×10^4 cells/well) and incubated overnight. Then, cells were exposed to BPQDs, BPQD-PEG and BPQD-PEG-TPP (internal BPQDs concentration of 4.0 μg/ml) for 24 h without irradiation. Afterwards, cells were resuspended and collected by centrifugation at 1000 rpm for 5 min, rinsed with ice cold PBS, and fixed with cold 70% ethanol at 4 °C for 24 h. The fixed cells were collected by centrifugation, washed with cold PBS, and resuspended in PI/RNase A dye working fluid for 30 min. The DNA content was measured by flow cytometry (NovoCyte 2060R, ACEA).

2.13. In vivo fluorescence imaging

Female BALB/c nude mice bearing Hela tumor were treated with an intravenous injection of BPQD-PEG-TPP@IR780 (100 μl, BPQDs concentration of 112.0 μg/ml) and monitored by a fluorescence imaging system (NightOWL II LB983, BERTHOLD) for 2, 12 and 24 h. Then, the tumor and main organs were collected and immediately imaged.

2.14. In vivo antitumor efficacy

The female BALB/c nude mice bearing Hela tumor were randomly divided into five groups ($n = 5$) according to the treatment: (1) Saline, (2) BPQD-PEG, (3) BPQD-PEG-TPP, (4) BPQD-PEG+NIR, (5) BPQD-PEG-TPP+NIR (all of them 100 μl at an equivalent BPQDs dose of 0.56 mg/kg) via intravenous injection after the average tumor volume reached ~100 mm^3 ($V = 0.5 \times \text{length} \times \text{width}^2$). Mice were irradiated with an 808 nm laser (1 W/cm^2, 10 min) 12 h post injection. The temperature changes and infrared thermographic maps were recorded by the infrared thermal image camera during the irradiation. Tumor volume and body weight were measured every 2 d until the mice were sacrificed at Day 14.

2.15. In vivo toxicity

Healthy female BALB/c nude mice were randomly divided into 3 groups ($n = 5$): (1) control group without any treatment, (2) BPQD-PEG-TPP intravenously injected for 1 d, (3) BPQD-PEG-TPP intravenously injected for 7 d. The injected dose of the BPQD-PEG-TPP was ~0.56 mg BPQDs per kg and hematological analyses were performed at 1 and 7 d post-injection.

2.16. Histopathological and immunohistochemical analysis

Mice were sacrificed at Day 14 and the tumor and major organs such as heart, liver, spleen, lung and kidney were collected and sliced for hematoxylin and eosin (H&E) staining. Thereafter, tumor sections were obtained for the terminal deoxynucleotidyl transferase-mediated deoxyuridine triphosphate nickend-labeling (TUNEL) assay and H&E staining.

2.17. Statistical analysis

The results were presented as means ± SEM, and statistical analysis was performed using a t-test and P value < 0.05 was considered to be statistically significant. $^*P < 0.05$; $^{**}P < 0.01$; $^{***}P < 0.001$.

3. Results and discussion

3.1. Morphology and characterization

To verify the coordination between BPQDs and AD-PEG-TPP, the UV absorption of BPQD-PEG-TPP synthesized with different AD-PEG-TPP / BPQDs feeding ratios (0.2, 0.5, 1.0, 2.0, 3.0 and 5.0) were used to measure the binding ratio (Fig. 2A

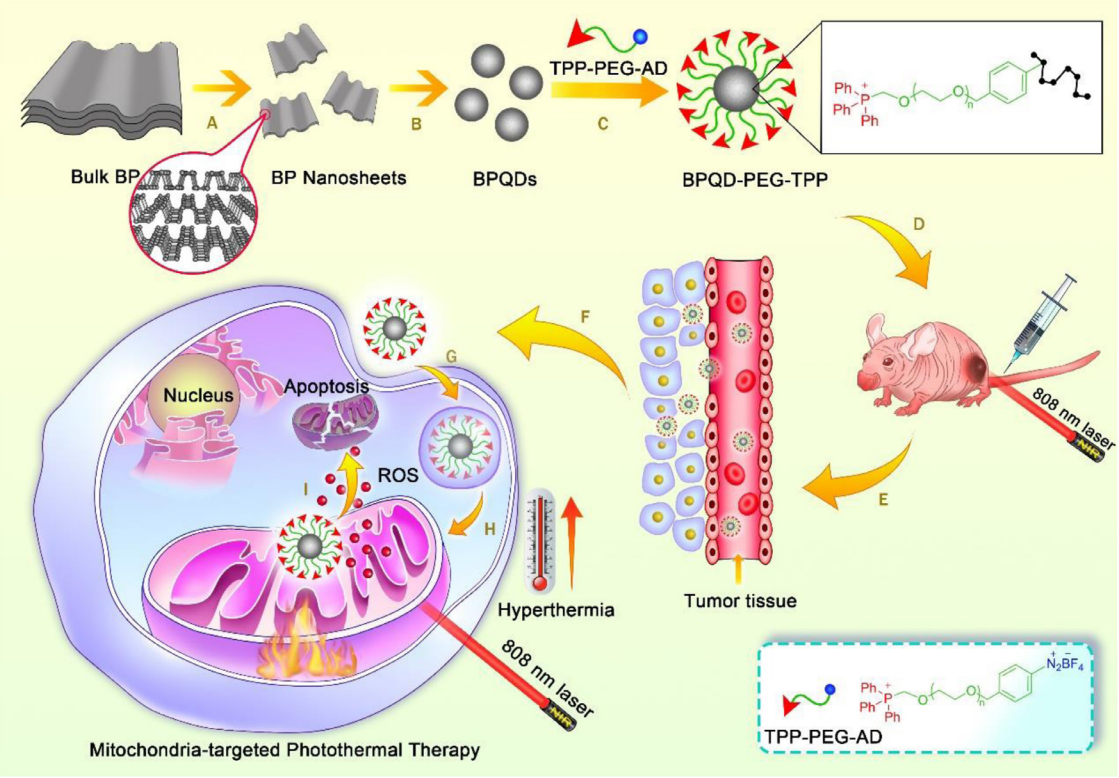

Fig. 1 – Schematic illustration of the preparation of BPQD-PEG-TPP for mitochondria-targeted PTT and the experimental design. (A) and (B) The preparation of BPQDs. (C) Synthesis of BPQD-PEG-TPP. (D) Intravenous injection of BPQD-PEG-TPP into tumor bearing Balb/c Nude mouse. (E) and (F) Accumulation of BPQD-PEG-TPP on tumor via EPR effect. (G) Endocytosis pathway of BPQD-PEG-TPP. (H) Mitochondria-targeted accumulation of BPQD-PEG-TPP. (I) ROS and hyperthermia induce tumor cell apoptosis.

and Fig. S1). Fig. 2A showed that, the binding ratio gradually increased with increasing AD-PEG-TPP/BPQDs feeding ratio, reaching a high ratio of 3.0. The amount of AD-PEG-TPP bound on the BPQDs surface was ~21.5% (w/w) of the BPQD-PEG-TPP, which was determined and converted by the UV absorbance of AD-PEG-TPP. Therefore, this binding ratio was applied to all subsequent experiments. The morphology of BPQDs before and after covalent grafting with AD-PEG-TPP was characterized by TEM and AFM. As shown in Fig. 2 B, the lateral size of BPQDs was 5–10 nm, and the AD-PEG-TPP covalent grafting did not change the morphology and structure of BPQDs (Fig. 2C). The BPQDs flake size distribution before and after covalent grafting was also analyzed by dynamic light scattering (DLS) spectroscopy in aqueous system. DLS analysis revealed that the particle diameter of the nano-materials increased from 8.76 nm (polydispersity is 0.196) to 25.37 nm (polydispersity is 0.195) after grafting (Fig. 2D), which may reduce the risk of renal filtration [10], owing to the extension of PEG chains in the aqueous environment [30–33]. Besides, after AD-PEG grafting, BPQD-PEG-TPP or BPQD-PEG was not easily filtered by the kidney *in vivo* due to the increase in particle sizes. The AFM images demonstrated that the thickness of BPQDs was less than 2 nm (Fig. 2E and 2F). However, after grafting, the morphology remained almost intact, while the height of the BPQD-PEG-TPP increased to ~6 nm (Fig. 2H and 2I). The increase in thickness could be attributed to a small amount of AD-PEG-TPP covalently bonded to the BPQDs surface [34]. Furthermore, after covalent grafting, the zeta potential of the BPQDs-based nanomaterials changed from -34.90 to -25.42 mV in DI water (Fig. S2), indicating that PEG has been successfully attached to the surface of BPQDs.

The successful covalent grafting with AD-PEG-TPP or AD-PEG was further confirmed with Raman spectral analysis, Fourier transform infrared (FTIR) spectra and X-ray photoelectron spectroscopy (XPS). Raman spectral analysis was performed to verify the structure of BPQD-PEG-TPP, which is considered as an effective method for sample identification through detailed rotation and vibration modes (Fig. 2G). BPQDs results showed peaks located at ~359.5, 436.6 and 463.2 cm^{-1} almost the same with those of bulk BP previously reported [10], which correspond to one out-of-plane phonon mode (A1 g) and two in-plane modes (B2 g and A2 g) of BP, indicating that the structure of prepared BPQDs did not change in comparison with the corresponding bulk BP. However, in BPQD-PEG-TPP, a slight shift to the low wavenumber could be observed, which could be attributed to a slight change in the ultrathin height after AD-PEG-TPP binding [8].

The formation of the C–P bonds that remarkably contributed to the stability of BP was driven by interaction between BPQDs and AD, in agreement with the literature [25]. However, the introduction of the TPP group resulted in a C–P

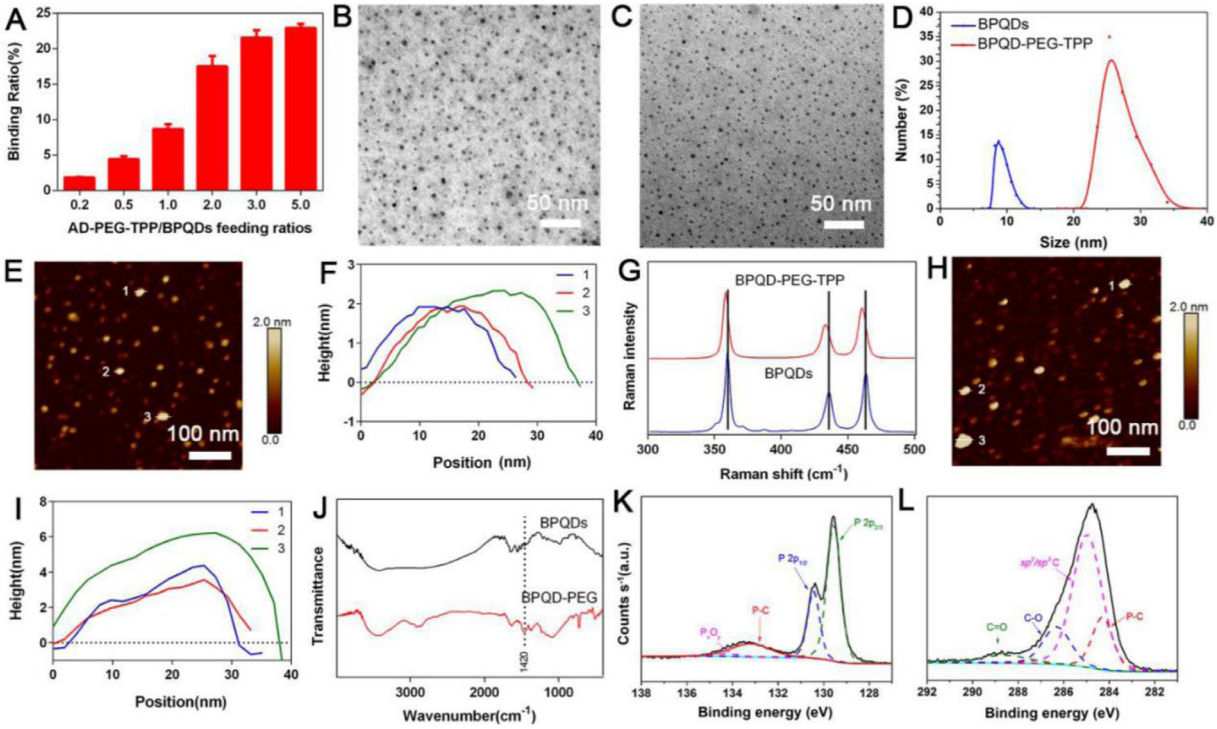

Fig. 2 – Preparation and characterizations of BPQD-based nanomaterials. (A) AD-PEG-TPP binding capacities on BPQDs (w/w) with increasing ratios between AD-PEG-TPP and BPQDs. (B) TEM, (E) AFM images, and (F) AFM measured thickness of BPQDs. (C) TEM, (H) AFM images, and (I) AFM measured thickness of BPQD-PEG-TPP. (D) Size distribution of BPQDs and BPQD-PEG-TPP as measured by DLS. (G) Raman spectra of BPQDs and BPQD-PEG-TPP. (J) FT-IR spectra of BPQDs and BPQD-PEG. (K) and (L) XPS spectra of BPQD-PEG.

bond between AD-PEG and BPQDs in the AD-PEG-TPP itself, thus, we mainly demonstrated the successful occurrence of the covalent grafting by analyzing the presence of new C-P bonds between AD-PEG and BPQDs. As shown in FTIR spectra (Fig. 2J), the peak at 1420 cm^{-1} could be due to the stretching vibration of C–P, confirming that BPQDs was successfully covalently grafted with AD-PEG [35]. Furthermore, XPS was conducted to study the intensity of C–P bonds. As shown by the P 2p XPS spectra in Fig. 2K, the broad peak at 133.23 eV corresponded to a P-C bond [19], confirming the new bond generation. Moreover, the P $2p_{2/3}$ and P $2p_{1/2}$ doublets were respectively located at 129.58 and 130.43 eV and were characteristic of BPQDs [12], while the P_xO_y peak was located at 134.23 eV. In Fig. 2L, the BPQD-PEG possessed the P–C peak located at 284.28 eV [25], further confirming the existence of the P–C bond, and the C=O and C–O peaks located at 288.63, 286.33, and 284.98 eV [19]. All these results demonstrated that the heterobifunctional PEG was successfully covalently grafted to the surface of BPQDs via C-P covalent bond.

3.2. *Stability and dispersibility evaluation under ambient conditions*

Considering that BPQDs-based nano-materials should circulate under physiological conditions for a long time before tumor PTT, its photothermal stability is of great significance [10]. The stability of BP could be significantly improved via binding with small molecule compounds, as it has been well documented. However, the binding ratio of high molecular polymer on BP is generally low, thus, whether the strategy could make BPQDs inert needs further verification. Therefore, the photothermal characteristics of BPQDs-based nanomaterials obtained after covalent grafting were first explored. At the beginning, the temperature of the BPQDs increased by 28.1 °C after for 10 min irradiation, but after 72 h, the temperature increased only by 5.6 °C due to the BPQDs rapid degradation (Fig. 3A). On the other hand, BPQD-PEG and BPQD-PEG-TPP were clearly more photothermally stable, and the temperature increase by 16.6 and 19.35 °C respectively even after 72 h (Fig. 3B and 3C). These results indicated that covalent grafting with AD could effectively retard the degradation of BPQDs and maintain the photothermal properties in DI water. In addition, photothermal conversion efficiency of BPQDs-based nanomaterials were also calculated. The η values of BPQD, BPQD-PEG and BPQD-PEG-TPP were 13.6%, 13.5% and 13.6%, respectively. It shows that the modification of the BPQDs didn't change its photothermal conversion ability.

After grafting, the temperature increments of BPQD-PEG-TPP were systematically explored at different concentrations and different laser power densities (Fig. 3D and 3E). The temperature of the BPQD-PEG-TPP quickly increased even at relatively low concentrations or low power density, indicating that the BPQD-PEG-TPP could promptly and efficiently

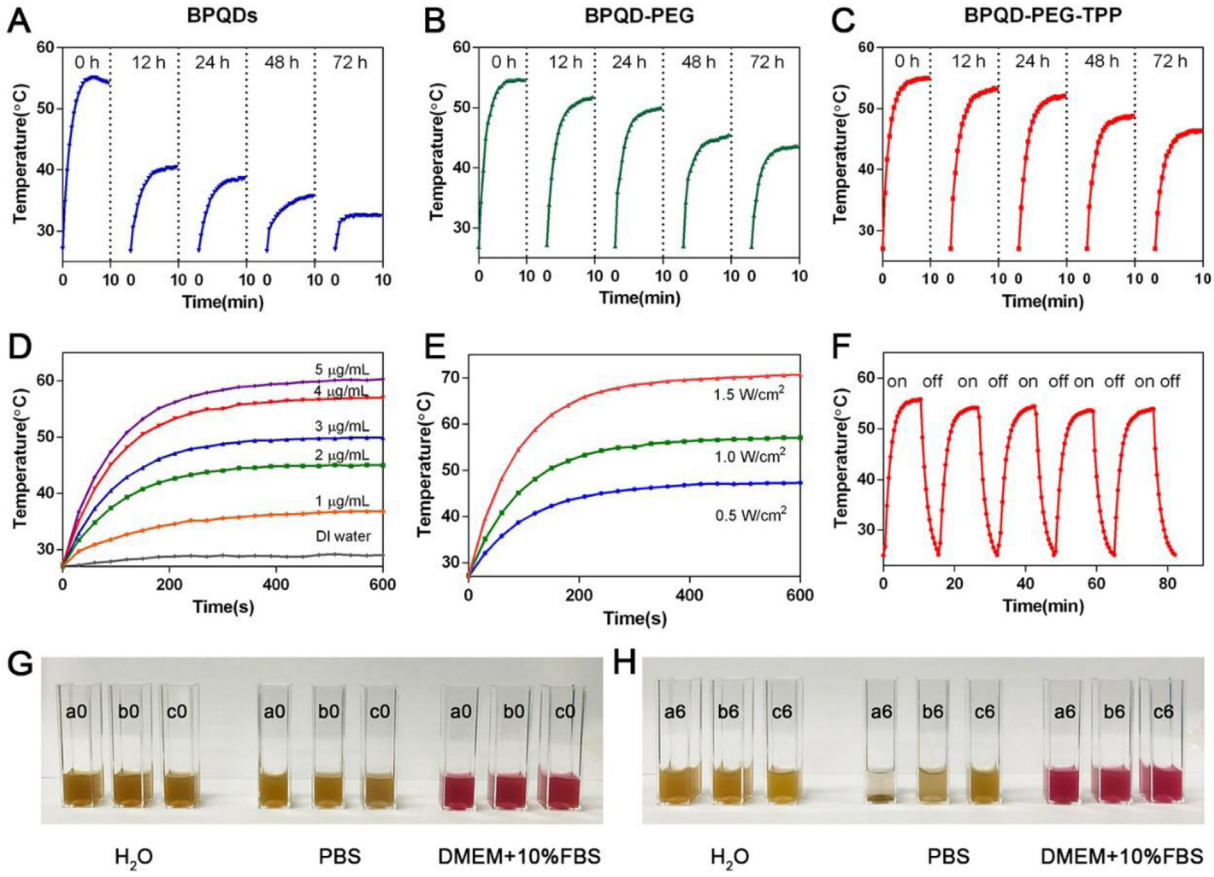

Fig. 3 – Photothermal stability and dispersibility of BPQD-PEG-TPP. (A-C) BPQDs, BPQD-PEG, and BPQD-PEG-TPP (internal BPQDs concentration of 4.0 μg/ml) dispersed in air-exposed water for 0, 12, 24, 72 h upon laser illumination (808 nm, 1.0 W/cm^2, 10 min). Photothermal heating profiles of BPQD-PEG-TPP in aqueous solution at (D) different concentrations (808 nm, 1.0 W/cm^2, 10 min) and (E) different power densities (4.0 μg/ml). (F) Heating of a suspension of the BPQD-PEG-TPP in water for five laser on/off cycles. (808 nm, 1.0 W/cm^2, 10 min). (G-H) Photos of BPQDs (a0, a6), BPQD-PEG (b0, b6), and BPQD-PEG-TPP (c0, c6) in DI water, PBS and DMEM with 10% FBS cell culture medium at 0 and 6 h.

convert NIR light energy into heat. To further evaluate the photostability of the BPQD-PEG-TPP, the temperature of a BPQD-PEG-TPP dispersion was detected under irradiation with a NIR laser on and off in five cycles (Fig. 3F). The photothermal effect of the BPQD-PEG-TPP did not weaken during the temperature increase, emphasizing their large potential as PTNAs. To evaluate the dispersity of PEG-grafted BPQDs, BPQDs, BPQD-PEG and BPQD-PEG-TPP with the same amount of BPQDs (4.0 μg/ml) were dispersed in DI water, PBS and DMEM containing 10% FBS for 6 h (Fig. 3G and 3H). Although BPQDs could disperse well in water, they quickly aggregated in the salt solution while PEG-grafted BPQDs still remained homogeneous. These results demonstrated that the dispersity of BPQD-PEG and BPQD-PEG-TPP was better than the one of BPQDs in PBS and DMEM.

3.3. *Mitochondria co-localization study*

To explore whether BPQD-PEG-TPP had the ability to localize at a subcellular level, NB-N_2 were used for subcellular tracking. The synthesis and fluorescence emission spectra of NB-N_2 shown in Fig. S4 and Fig. S5. First, different incubation times with the same NB-BPQD-PEG-TPP concentration were used. As shown in Fig. S6, the red fluorescence of HeLa cells gradually enhanced with the increase of the incubation time. However, the fluorescence intensity at 4 h and 6 h incubation was not much different, thus, 4 h was chosen as the optimal incubation time. Next, DiO, Hoechst 33342, LysoTracker Green and MitoTracker Green commercial dyes were used to stain the cell membrane, nuclei, lysosomes and mitochondria, respectively. As shown in Fig. 4A and 4B, the green fluorescence of DiO and the blue fluorescence of Hoechst 33342 were hardly overlapping with the red fluorescence of NB-BPQD-PEG-TPP, demonstrating that NB-BPQD-PEG-TPP was not able to localize in the plasma membrane and nucleus. Moreover, most of the LysoTracker Green fluorescence was merged with the red fluorescence of NB-BPQD-PEG-TPP (Fig. 4C), indicating the endocytosis of NB-BPQD-PEG-TPP on HeLa cells [36]. Importantly, as shown in Fig. 4D, the green fluorescence of MitoTracker Green and the red fluorescence of NB-BPQD-PEG-TPP were merged, confirming the excellent subcellular targeting ability of NB-BPQD-PEG-TPP to mitochondria. Moreover, we compared the intracellular localization of NB-BPQD-PEG-TPP and NB-BPQD-

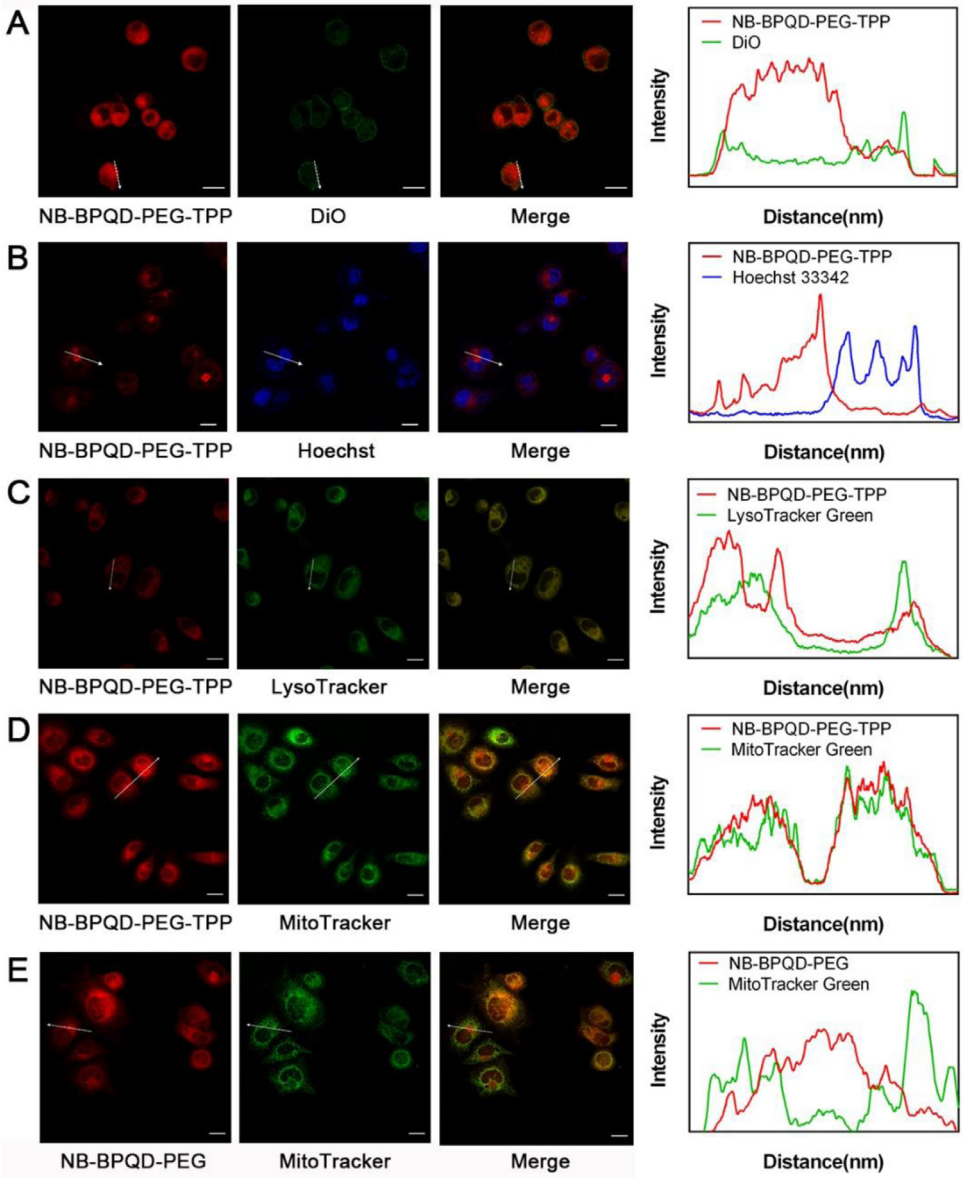

Fig. 4 – The subcellular localizations of NB-BPQD-PEG-TPP. CLSM images and the corresponding fluorescence profile analysis of HeLa cells after treatment with NB-BPQD-PEG-TPP (2.0 μg/ml) for 4 h and stained by (A) DiO, (B) Hoechst 33342, (C) LysoTracker Green and (D) MitoTracker Green. (E) The subcellular localizations of NB-BPQD-PEG and MitoTracker Green. Scale bar: 20 μm.

PEG in HeLa cells. The control sample NB-BPQD-PEG due to the absence of the TPP moiety, was randomly distributed in the cells, and a non-specific colocalization effect to mitochondria could be observed (Fig. 4E). Same results were found in MCF-7 cells treated with NB-BPQD-PEG and NB-BPQD-PEG-TPP (Fig. S7). The mitochondria co-localization results indicated the presence of the TPP moiety in the BPQD-PEG-TPP, and that BPQD-PEG-TPP could enter the cytoplasm by endocytosis reaching mitochondria. Thus, their targeting ability was still present even in different cells. This precise subcellular localization of BPQD-PEG-TPP could significantly improve the PTT efficiency because mitochondria are susceptible to ROS and hyperthermia.

3.4. *In vitro cytotoxicity assay and mechanism study*

Thanks to their good mitochondria-targeted ability, the photothermal effect of BPQD-PEG-TPP was evaluated. The *in vitro* cytotoxicity and consequent PTT efficiency of the BPQDs-based nanomaterials was evaluated on normal (HDF cells) and cancer cells (HeLa cells) in air-exposed water after 24 h. As shown in Fig. 5A, the BPQDs, BPQD-PEG, and BPQD-PEG-TPP (internal BPQDs concentration of 0, 1.0, 2.0, 4.0, 10.0 μg/ml) had a weak effect on HDF cell viability without irradiation even at the internal BPQDs concentration of 10.0 μg/ml, which was far beyond the one applied in the following experiments. Moreover, no difference in HeLa cell viability was

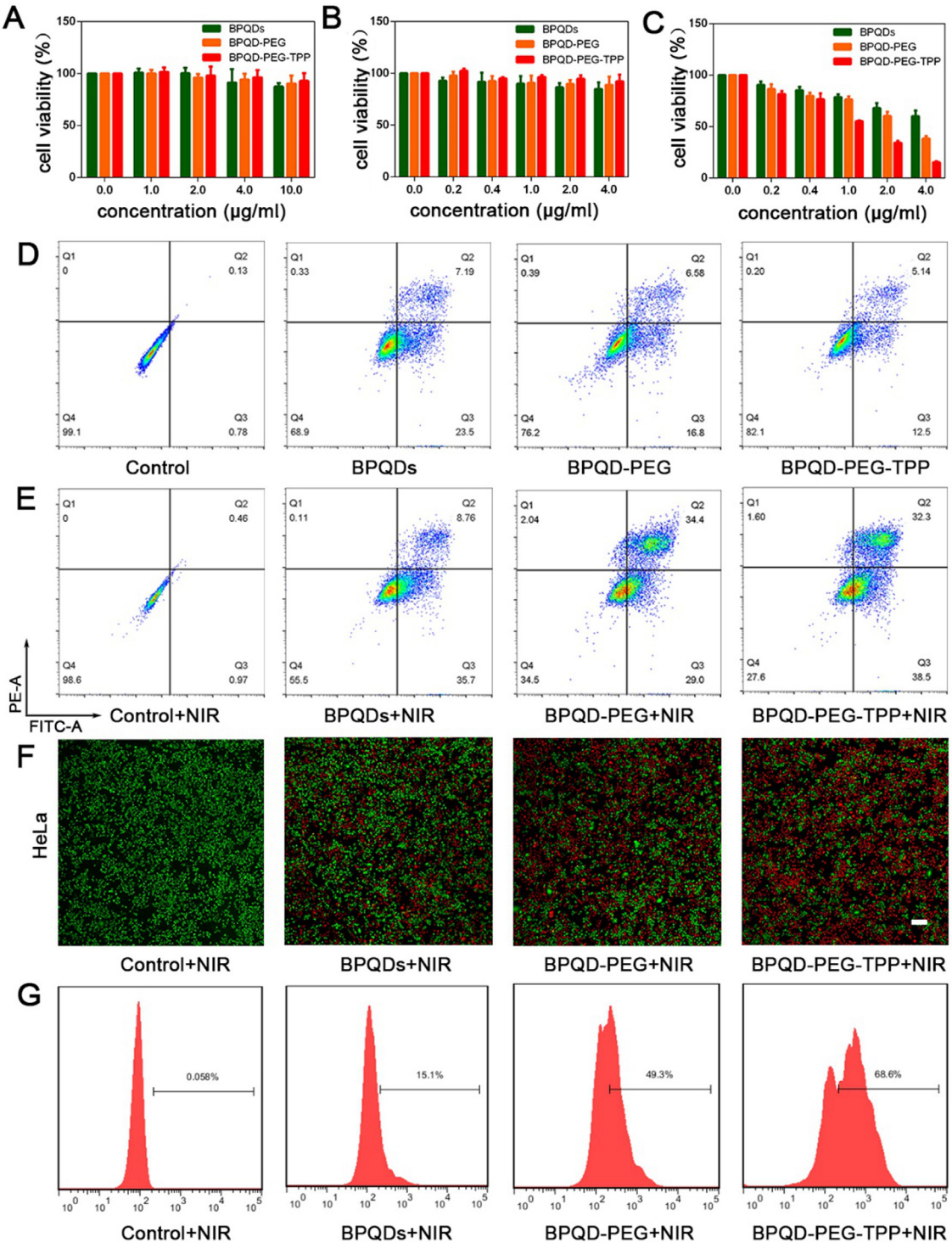

Fig. 5 – Photothermal therapy efficiency *in vitro* with BPQD-PEG-TPP. (A) Cell viability of HDF cells incubated with BPQDs, BPQD-PEG, and BPQD-PEG-TPP at different BPQDs concentrations without laser irradiation. Cell viability of HeLa cells incubated with BPQDs, BPQD-PEG, and BPQD-PEG-TPP at different BPQDs concentrations (B) without and (C) with laser irradiation (808 nm, 1.0 W/cm^2, 10 min). Data represent mean ± SEM ($n = 5$). (D) Flow cytometry studies of HeLa cells incubated without nanoparticles and with BPQDs, BPQD-PEG, and BPQD-PEG-TPP at a BPQDs concentration of 4.0 μg/ml without laser illumination. (E) Flow cytometry studies of HeLa cells incubated without nanoparticles and with BPQDs, BPQD-PEG, and BPQD-PEG-TPP at a BPQDs concentration of 4.0 μg/ml with laser irradiation (808 nm, 1.0 W/cm^2, 10 min). (F) Fluorescence images of the Calcein-AM (green, live cells) and PI (red, dead cells) co-stained HeLa cells after exposed to laser irradiation (808 nm, 1.0 W/cm^2, 10 min) following treatment with different BPQDs formulations (BPQDs concentration of 4.0 μg/ml). Scale bar = 200 μm. (G) ROS generation in HeLa cells after incubation with different BPQDs formulations (BPQDs concentration of 2.0 μg/ml) with laser irradiation (808 nm, 1.0 W/cm^2, 10 min).

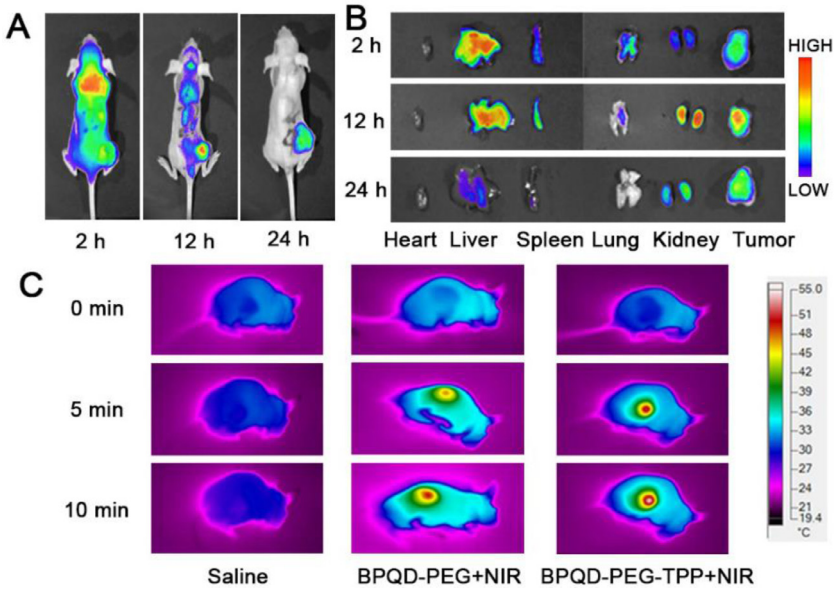

Fig. 6 – *In vivo* fluorescence and photothermal imaging of BPQD-PEG-TPP. (A) *In vivo* fluorescence imaging of tumor-bearing mice after BPQD-PEG-TPP@IR780 injection. (B) *Ex vivo* fluorescence imaging of major organs and tumors after systemically administration at different time. (C) IR thermal imaging of mice after injection of Saline, BPQD-PEG and BPQD-PEG-TPP under laser illumination for 10 min.

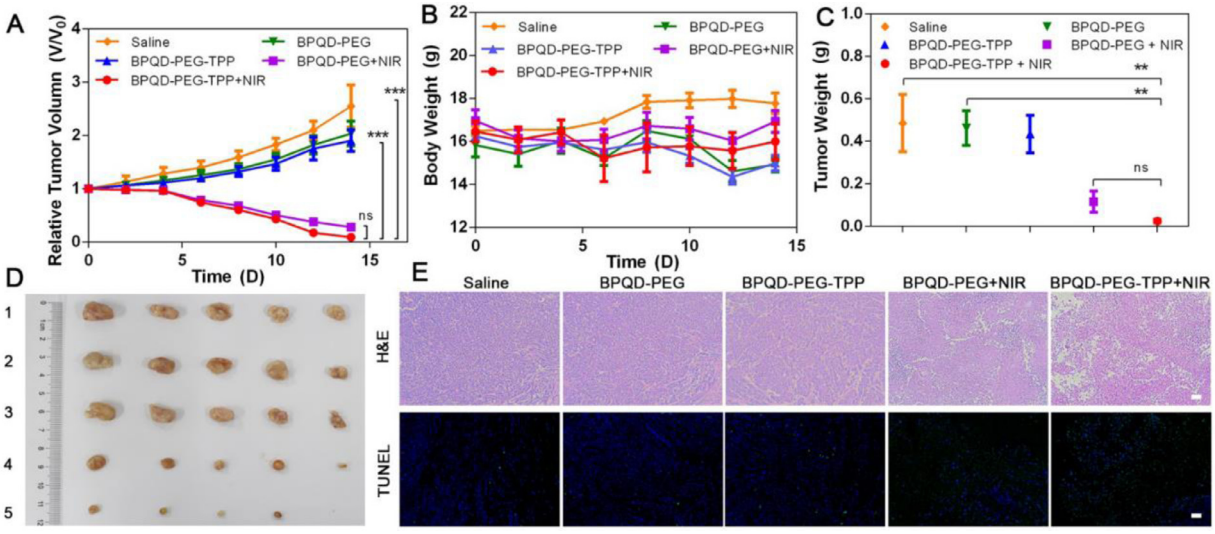

Fig. 7 – *In vivo* antitumor effect of BPQD-PEG-TPP. (A) Relative tumor volume with time dependent after treatments with different BPQDs formulations ($n = 5$, mean ± SEM, ***$P < 0.001$). (B) Body weight changes of each group in 14 d. (C) Tumor weight of each group at Day 14 ($n = 5$, mean ± SEM, **$P < 0.01$). (D) Imaging of tumors after treated with various formulations. (E) H&E stained tumor slices and TUNEL analysis of tumor tissues at day 14 after treatment with saline, and BPQDs-based nanomaterials (scale bar, 100 μm for all panels).

observed when the cells were incubated with BPQDs, BPQD-PEG and BPQD-PEG-TPP (internal BPQDs concentration of 0, 0.2, 0.4, 1.0, 2.0 and 4.0 μg/ml) the concentration gradient from 0 μg/ml to 4.0 μg/ml without laser irradiation (Fig. 5B), indicating the excellent biocompatibility of the three nanomaterials. Furthermore, the relative viability of HeLa cells gradually decreased with the increasing concentration under laser irradiation (Fig. 5C). In detail, when the internal BPQDs concentration was 2.0 μg/ml, 66% of cells were killed after the treatment with BPQD-PEG-TPP, which was much higher than the percentage of those treated with BPQD-PEG (40% cell death) and BPQDs (32% cell death). With the increasing concentration, the antitumor efficacy of BPQD-PEG-TPP was increasing. At 4.0 μg/ml BPQDs, nearly 85% of cells were killed after NIR irradiation. Nevertheless, at the same concentration, more than 38% BPQD-PEG and 60% BPQDs treated HeLa

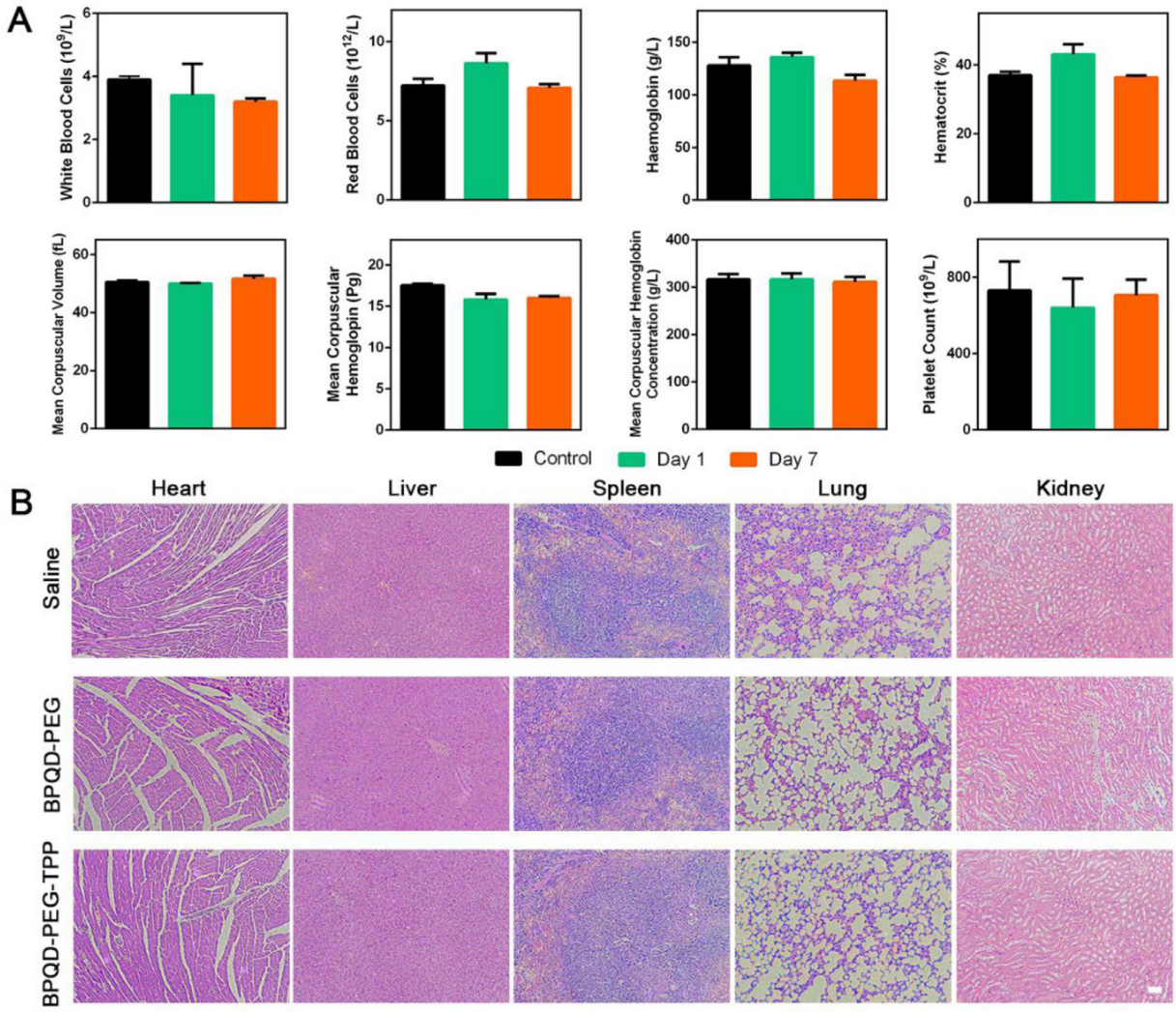

Fig. 8 – *In vivo* toxicity of BPQD-PEG-TPP. (A) Haematological data of the mice intravenously injected with the BPQD-PEG-TPP at 1 and 7 d post-injection. The terms are following: white blood cells, red blood cells, haemoglobin, haematocrit, mean corpuscular volume, mean corpuscular haemoglobin, mean corpuscular haemoglobin concentration, platelet count. The blood of untreated healthy Balb/c mice were used as control. (B) H&E stained histological images of tissue sections from major organs after 14 d of treatment with BPQD-PEG, BPQD-PEG-TPP. Saline was used as a control (scale bar, 100 μm for all panels).

cells were still alive. Notably, BPQD-PEG-TPP showed an excellent photothermal effect, and its photothermal toxicity was stronger than that of BPQD-PEG and BPQDs, which could be attributed to its mitochondria targeting PTT cytotoxicity.

As shown in Fig. 5D and 5E, the percentage of cells that underwent apoptosis after treatment with BPQD-PEG-TPP after irradiation was 70.8% which was quite higher than the apoptotic value in the group without NIR irradiation (17.64%). In addition, the percentage of cells that underwent apoptosis after the treatment with BPQD-PEG with and without irradiation was 63.4% and 23.38%, respectively. Furthermore, BPQDs killed 44.46% of cells under irradiation and 30.69% without irradiation. Obviously, the flow cytometry analysis revealed that BPQD-PEG-TPP exerted a more effective phototherapeutic effect than that exerted by BPQD-PEG and BPQDs. Similar results were observed from the fluorescence imaging (Fig. 5F and Fig. S8) of the cells co-stained by Calcein-AM/PI. BPQD-PEG-TPP showed better phototherapeutic effects than BPQD-PEG and BPQDs, which could be attributed to the mitochondria-targeted PTT efficacy.

All the above results indicated that BPQD-PEG-TPP had a negligible toxicity, inhibited tumor growth and caused tumor cell apoptosis. In order to further explore its mechanism, the generation of ROS and the cell cycle we further evaluated. As shown in Fig. 5G, HeLa cells treated with BPQD-PEG-TPP showed the highest ROS production (68.6%), which was much higher than the ROS produced by the cells treated with BPQD-PEG (49.3%) and BPQDs (15.1%). These results demonstrated that BPQD-PEG-TPP could trigger ROS production in mitochondria and induce cell apoptosis under NIR irradiation. To further investigate whether the nanomaterials induced an efficient cycle arrest on tumor cells,

cell cycle analysis was performed on cells treated with BPQDs-based nano-materials. As shown in Fig. S9, HeLa cells treated with all the three BPQDs-based nano-materials without NIR irradiation resulted in a significant increase of S and G2/M phase cells. In contrast, the cell cycle distribution of HDF cells was almost unchanged. These results indicated that BPQDs-based materials could indeed inhibit cell proliferation and induce cell apoptosis in tumor cells, which is consistent with previous reports [37]. Therefore, based on these results, we could confirm that BPQD-PEG-TPP has the most excellent antitumor ability *in vitro* via hyperthermia and ROS production, exhibiting the advantages of mitochondria-targeted photothermal cancer therapy.

3.5. *In/Ex vivo imaging and NIR thermal imaging*

The *in/ex vivo* fluorescence and IR thermal imaging of the BPQDs-based nanomaterials was further investigated. First, *in vivo* distribution and tumor accumulation experiments were carried out to understand the dynamic distribution of the BPQD-PEG-TPP@IR780 in HeLa tumor-bearing nude mice at specific time points. As shown in Fig. 6A, BPQD-PEG-TPP@IR780 were rapidly distributed throughout the whole body at 2 h after intravenous injection and emitted strong fluorescence signals. The intensity gradually increased in the tumor region at 12 h after injection, indicating that BPQD-PEG-TPP@IR780 could efficiently accumulate in the tumor region. Moreover, strong fluorescent signals could still be found in the tumor tissues at 24 h post injection although the fluorescence signals declined in the body, demonstrating a superior tumor accumulation of BPQD-PEG-TPP through the EPR effect. Furthermore, major organs and tumors were resected at determined time points. *Ex vivo* fluorescence imaging showed a strong fluorescence in the tumor tissue, liver and kidney, suggesting a good tumor targeting and effective catabolism of BPQD-PEG-TPP@IR780 (Fig. 6B).

Mice IR thermal images are shown in Fig. 6C. The tumor temperature of the BPQD-PEG-TPP group rapidly increased to 52.71 °C after 10 min of NIR irradiation, which was high enough for an effective tumor ablation. Moreover, the tumor temperature of the BPQD-PEG-TPP group was slightly higher than that of BPQD-PEG group (49.45 °C), whereas the tumor treated with saline did not show a high temperature increase after 10 min of laser irradiation. These results indicated that BPQD-PEG-TPP possessed excellent photothermal characteristic *in vivo*.

3.6. *In vivo PTT performance*

To further evaluate the potential of BPQDs nanomaterials for *in vivo* mitochondria-targeted PTT in cancer therapy, Balb/c nude mice bearing HeLa tumors were established. The tumor growth was markedly inhibited after intravenous injection of BPQDs-based nanomaterials and NIR irradiation exposure, and especially the BPQD-PEG-TPP + NIR group showed a small relative tumor volume as expected (Fig. 7A—7C). On the contrary, non-irradiation treatment of tumor-bearing mice with BPQDs-based nanomaterials resulted in a not significant inhibition of tumor growth compared with PBS-treated mice. Furthermore, no significant body weight loss was observed in all groups, suggesting negligible side effects on the mice (Fig. 7D). Overall, BPQDs-based nanomaterials showed excellent photothermal anti-tumor effects and biocompatibility *in vivo*. H&E staining and TUNEL assay were used to analyze cell necrosis and apoptosis in tumor tissues after different treatments. In Fig. 7E, BPQD-PEG-TPP+ NIR was the most effective in inducing tumor necrosis and TUNEL-positive tumor cells [38–40]. These results indicated that the mitochondria-targeted PTT could induce cancer cell death by inducing necrosis and apoptosis in the tumor. The *in vivo* toxicology of the BPQD-PEG-TPP was systematically explored. The standard hematology markers including white blood cells count, red blood cells count, hemoglobin, hematocrit, mean corpuscular volume, mean corpuscular hemoglobin, mean corpuscular hemoglobin concentration, and platelet count were measured (Fig. 8A) [10]. All these parameters were normal in the BPQD-PEG-TPP group (1 and 7 d post-injection) compared with the control group. These results indicated that the treatment with BPQD-PEG-TPP did not cause a significant infection and inflammation in the treated mice. Finally, tissues from major organs such as heart, liver, spleen, lung, and kidney were stained with H&E to observe potential histological changes (Fig. 8B). No apparent organ damage was observed in all groups throughout the entire treatment period, indicating no significant histological abnormalities or lesions of the tested dose.

4. Conclusions

In summary, a simple and efficient heterobifunctional PEG-grafted BPQDs was constructed and exhibited excellent tumor mitochondria-targeted PTT effects. By covalently grafting polymer AD-PEG-TPP on the surface of BPQDs, the stability and dispersibility of the nanomaterials under physiological conditions were improved, maintaining the remarkable photothermal properties of BPQDs. Furthermore, excellent mitochondria-targeting ability of BPQDs was also presented through TPP moiety, which exhibited much more photothermal cytotoxicity *in vitro and in vivo* by inducing ROS generation. This simple polymer-grafting “three-in-one” strategy might be a promising strategy for BPQDs in the field of mitochondria-targeted photothermal cancer therapy.

Author contributions

Deng WB, Liu G and Mei L conceived the idea and whole experimental project. Qi JY, Xiong Y and Cheng K carried out the synthesis, characterization and data analysis. Huang Q, Cao JX and He FM assisted with data analysis and interpretation. Qi JY wrote the manuscript. Deng WB, Mei L and Liu G provided revisions.

Conflict of interest

The authors declare no competing interests.

Acknowledgements

We are grateful for the financial support from National Natural Science Foundation of China (51703258, 81772449 and 81971081), Guangzhou science technology and innovation commission (201804010309 and 201803010090), Science, Technology & Innovation Commission of Shenzhen Municipality (JCYJ20180307154606793 and JCYJ20180507181654186).

Supplementary materials

Supplementary material associated with this article can be found, in the online version, at doi:10.1016/j.ajps.2020.09.001.

REFERENCES

[1] Huang X, El-Sayed IH, Qian W, El-Sayed MA. Cancer cell imaging and photothermal therapy in the near-infrared region by using gold nanorods. J Am Chem Soc 2006;128(6):2115–20.
[2] Zha Z, Yue X, Ren Q, Dai Z. Uniform polypyrrole nanoparticles with high photothermal conversion efficiency for photothermal ablation of cancer cells. Adv Mater 2013;25(5):777–82.
[3] Cheng L, Wang C, Feng L, Yang K, Liu Z. Functional nanomaterials for phototherapies of cancer. Chem Rev 2014;114(21):10869–939.
[4] Cheng W, Nie J, Gao N, Liu G, Tao W, Xiao X, et al. A multifunctional nano-platform against multidrug resistant cancer: merging the best of targeted chemo/gene/photothermal therapy. Adv Funct Mater 2017;27(45):1704135.
[5] Liu G, Tsai HI, Zeng X, Qi J, Luo M, Wang X, et al. Black phosphorus nanosheets-based stable drug delivery system via drug-self-stabilization for combined photothermal and chemo cancer therapy. Chem Eng J 2019;375:121917.
[6] Liu H, Neal AT, Zhu Z, Luo Z, Xu X, Tomanek D, et al. Phosphorene: an unexplored 2D semiconductor with a high hole mobility. ACS Nano 2014;8(4):4033–41.
[7] Qiu M, Ren WX, Jeong T, Won M, Park GY, Sang DK, et al. Omnipotent phosphorene: a next-generation, two-dimensional nanoplatform for multidisciplinary biomedical applications. Chem Soc Rev 2018;47(15):5588–601.
[8] Tao W, Zhu X, Yu X, Zeng X, Xiao Q, Zhang X, et al. Black phosphorus nanosheets as a robust delivery platform for cancer theranostics. Adv Mater 2017;29(1):1603279.
[9] Huang Y, Qiao J, He K, Bliznakov S, Sutter E, Chen X, et al. Interaction of black phosphorus with oxygen and water. Chem Mater 2016;28(22):8330–9.
[10] Shao J, Xie H, Huang H, Li Z, Sun Z, Xu Y, et al. Biodegradable black phosphorus-based nanospheres for *in vivo* photothermal cancer therapy. Nat Commun 2016;7:12967.
[11] Childers DL, Corman J, Edwards M, Elser JJ. Sustainability challenges of phosphorus and food: solutions from closing the human phosphorus cycle. BioScience 2011;61(2):117–24.
[12] Sun Z, Xie H, Tang S, Yu XF, Guo Z, Shao J, et al. Ultrasmall black phosphorus quantum dots: synthesis and use as photothermal agents. Angew Chem Int Edit 2015;54(39):11526–30.
[13] Zhang Y, Zhang L, Wang Z, Wang F, Kang L, Cao F, et al. Renal-clearable ultrasmall covalent organic framework nanodots as photodynamic agents for effective cancer therapy. Biomaterials 2019;223:119462.
[14] Zhou Q, Chen Q, Tong Y, Wang J. Light-induced ambient degradation of few-layer black phosphorus: mechanism and protection. Angew Chem Int Edit 2016;55(38):11437–41.
[15] Wang G, Slough WJ, Pandey R, Karna SP. Degradation of phosphorene in air: understanding at atomic level. 2D Mater 2016;3(2):025011.
[16] Abellan G, Lloret V, Mundloch U, Marcia M, Neiss C, Gorling A, et al. Noncovalent functionalization of black phosphorus. Angew Chem Int Edit 2016;55(47):14557–62.
[17] Zhao Y, Wang H, Huang H, Xiao Q, Xu Y, Guo Z, et al. Surface coordination of black phosphorus for robust air and water stability. Angew Chem Int Edit 2016;55(16):5003–7.
[18] Zeng X, Luo M, Liu G, Wang X, Tao W, Lin Y, et al. Polydopamine-modified black phosphorous nanocapsule with enhanced stability and photothermal performance for tumor multimodal treatments. Adv Sci 2018;5(10):1800510.
[19] Zhao Y, Tong L, Li Z, Yang N, Fu H, Wu L, et al. Stable and multifunctional dye-modified black phosphorus nanosheets for near-infrared imaging-guided photothermal therapy. Chem Mater 2017;29(17):7131–9.
[20] Chen W, Tian X, He W, Li J, Feng Y, Pan G. Emerging functional materials based on chemically designed molecular recognition. BMC Materials 2020;2:1.
[21] Liu Z, Robinson JT, Sun X, Dai H. PEGylated nanographene oxide for delivery of water-insoluble cancer drugs. J Am Chem Soc 2008;130(33):10876–7.
[22] Prencipe G, Tabakman SM, Welsher K, Liu Z, Goodwin AP, Zhang L, et al. PEG branched polymer for functionalization of nano-materials with ultralong blood circulation. J Am Chem Soc 2009;131(13):4783–7.
[23] Natarajan S, Harini K, Gajula GP, Sarmento B, Neves-Petersen MT, Thiagarajan V. Multifunctional magnetic iron oxide nanoparticles: diverse synthetic approaches, surface modifications, cytotoxicity towards biomedical and industrial applications. BMC Materials 2019;1(2).
[24] Qian Y, Shen Y, Deng S, Liu T, Qi F, Lu Z, et al. Dual functional β-peptide polymer-modified resin beads for bacterial killing and endotoxin adsorption. BMC Materials 2019;1(5).
[25] Ryder CR, Wood JD, Wells SA, Yang Y, Jariwala D, Marks TJ, et al. Covalent functionalization and passivation of exfoliated black phosphorus via aryl diazonium chemistry. Nat Chem 2016;8(6):597–602.
[26] Jung HS, Lee JH, Kim K, Koo S, Verwilst P, Sessler JL, et al. A mitochondria-targeted cryptocyanine-based photothermogenic photosensitizer. J Am Chem Soc 2017;139(29):9972–8.
[27] Tan X, Luo S, Long L, Wang Y, Wang D, Fang S, et al. Structure-guided design and synthesis of a mitochondria-targeting near-infrared fluorophore with multimodal therapeutic activities. Adv Mater 2017;29(43):1704196.
[28] Wang H, Chang J, Shi M, Pan W, Li N, Tang B. A dual-targeted organic photothermal agent for enhanced photothermal therapy. Angew Chem Int Edit 2019;58(4):1057–61.
[29] Yang X, Wang D, Zhu J, Xue L, Ou C, Wang W, et al. Functional black phosphorus nanosheets for mitochondria-targeting photothermal/photodynamic synergistic cancer therapy. Chem Sci 2019;10(13):3779–85.
[30] Liu G, Hi Tsai, Zeng X, Zuo Y, Tao W, Han J, et al. Phosphorylcholine-based stealthy nanocapsules enabling tumor microenvironment-responsive doxorubicin release for tumor suppression. Theranostics 2017;7(5):1192–203.
[31] Wang S, Liu X, Chen S, Liu Z, Zhang X, Liang XJ, et al. Regulation of Ca(2+) signaling for drug-resistant breast

cancer therapy with mesoporous silica nanocapsule encapsulated doxorubicin/siRNA cocktail. ACS Nano 2019;13(1):274–83.
[32] Liu G, Ma R, Ren J, Li Z, Zhang H, Zhang Z, et al. A glucose-responsive complex polymeric micelle enabling repeated on–off release and insulin protection. Soft Matter 2013;9(5):1636–44.
[33] Liu G, Gao H, Zuo Y, Zeng X, Tao W, Tsai HI, et al. DACHPt-loaded unimolecular micelles based on hydrophilic dendritic block copolymers for enhanced therapy of lung cancer. ACS Appl Mater Interfaces 2017;9(1):112–9.
[34] Tao W, Zhu X, Yu X, Zeng X, Xiao Q, Zhang X, et al. Black phosphorus nanosheets as a robust delivery platform for cancer theranostics. Adv Mater 2017;29(1):1603276.
[35] Liu H, Tao L, Zhang Y, Xie C, Zhou P, Liu H, et al. Bridging covalently functionalized black phosphorus on graphene for high-performance sodium-ion battery. ACS Appl Mater Interfaces 2017;9(42):36849–56.
[36] Hu Q, Gao M, Feng G, Liu B. Mitochondria-targeted cancer therapy using a light-up probe with aggregation-induced-emission characteristics. Angew Chem Int Edit 2014;53(51):14225–9.
[37] Zhou W, Pan T, Cui H, Zhao Z, Chu PK, Yu XF. Black phosphorus: bioactive nanomaterials with inherent and selective chemotherapeutic effects. Angew Chem Int Edit 2018;58:779–84.
[38] Wang H, Yang X, Shao W, Chen S, Xie J, Zhang X, et al. Ultrathin black phosphorus nanosheets for efficient singlet oxygen generation. J Am Chem Soc 2015;137(35):11376–82.
[39] Shi Z, Zhou Y, Fan T, Lin Y, Zhang H, Mei L. Inorganic nano-carriers based smart drug delivery systems for tumor therapy. Smart Materials in Medicine 2020;1:32–47.
[40] Shi Z, Li Q, Mei L. pH-Sensitive nanoscale materials as robust drug delivery systems for cancer therapy. Chinese Chemical Letters 2020;31(6):1345–56.